

Fused Ultrasound And Electromyography-Driven Neuromuscular Model To Improve Plantarflexion Moment Prediction Across Walking Speeds

Qiang Zhang

University of North Carolina-Chapel Hill and North Carolina State University <https://orcid.org/0000-0002-8806-9672>

Natalie Fragnito

University of North Carolina-Chapel Hill and North Carolina State University

Jason R. Franz

University of North Carolina-Chapel Hill and North Carolina State University

Nitin Sharma (✉ nsharm23@ncsu.edu)

University of North Carolina-Chapel Hill and North Carolina State University <https://orcid.org/0000-0003-1872-0156>

Research

Keywords: B-mode ultrasound imaging, surface electromyography, muscle thickness, net plantarflexion moment, treadmill walking, neuromuscular model

Posted Date: January 11th, 2022

DOI: <https://doi.org/10.21203/rs.3.rs-1136552/v1>

License:  This work is licensed under a Creative Commons Attribution 4.0 International License.

[Read Full License](#)

Fused Ultrasound and Electromyography-driven Neuromuscular Model to Improve Plantarflexion Moment Prediction across Walking Speeds

Qiang Zhang^{1,2}, Natalie Fragnito^{1,2}, Jason R Franz^{1,2} and Nitin Sharma^{1,2*}

*Correspondence:

nsharm23@ncsu.edu

¹Joint Department of Biomedical Engineering at the University of North Carolina-Chapel Hill and North Carolina State University, 1840 Entrepreneur Dr., 27695 Raleigh, NC, USA

Full list of author information is available at the end of the article

Abstract

Background: Improving the prediction ability of a human-machine interface (HMI) is critical to accomplish a bio-inspired or model-based control strategy for rehabilitation interventions, which are of increased interest to assist limb function post neurological injuries. A fundamental role of the HMI is to accurately predict human intent by mapping signals from a mechanical sensor or surface electromyography (sEMG) sensor. These sensors are limited to measuring the resulting limb force or movement or the neural signal evoking the force. As the intermediate mapping in the HMI also depends on muscle contractility, a motivation exists to include architectural features of the muscle as surrogates of dynamic muscle movement, thus further improving the HMI's prediction accuracy.

Objective: The purpose of this study is to investigate a non-invasive sEMG and ultrasound (US) imaging-driven Hill-type neuromuscular model (HNM) for net ankle joint plantarflexion moment prediction. We hypothesize that the fusion of signals from sEMG and US imaging results in a more accurate net plantarflexion moment prediction than sole sEMG or US imaging.

Methods: Ten young non-disabled participants walked on a treadmill at speeds of 0.50, 0.75, 1.00, 1.25, and 1.50 m/s. The proposed HNM consists of two muscle-tendon units. The muscle activation for each unit was calculated as a weighted summation of the normalized sEMG signal and normalized muscle thickness signal from US imaging. The HNM calibration was performed under both single-speed mode and inter-speed mode, and then the calibrated HNM was validated across all walking speeds.

Results: On average, the normalized moment prediction root mean square error was reduced by 14.58 % ($p = 0.012$) and 36.79 % ($p < 0.001$) with the proposed HNM when compared to sEMG-driven and US imaging-driven HNMs, respectively. Also, the calibrated models with data from the inter-speed mode were more robust than those from single-speed modes for the moment prediction.

Conclusions: The proposed sEMG-US imaging-driven HNM can significantly improve the net plantarflexion moment prediction accuracy across multiple walking speeds. The findings imply that the proposed HNM can be potentially used in bio-inspired control strategies for rehabilitative devices due to its superior prediction.

Keywords: B-mode ultrasound imaging; surface electromyography; muscle thickness; net plantarflexion moment; treadmill walking; neuromuscular model

Background

Locomotion mobility accounts for a dominant part of human activities of daily living, like moving around the home and community, going to work or school, doing errands, visiting friends, etc. The human lower extremity plays an essential role in achieving locomotion mobility. The human ankle plantarflexors generate a large burst of “push-off” mechanical power during the late stance phase of walking, enabling forward and upward acceleration of the body’s center of mass. Due to neurological disorders or injuries like spinal cord injury, stroke, and multiple sclerosis, the weakened function or dysfunction of plantarflexors is likely to cause a dramatic decrease in the “push-off” power. Consequently, these mobility disorders impair walking function and cause poor energy economy [1], as well as disrupt both physical and emotional well-being [2].

Modern neurorehabilitation devices, such as powered ankle exoskeletons [3–5], soft exosuits [6, 7], and functional electrical stimulation [8–12], may use assist-as-needed control to actively engage and maximize recovery of users with mobility impairments [13, 14]. In turn, the efficacy of the control strategy depends on the accurate determination of continuous human volitional movement intent (net joint moment). Mechanical sensors, like force or torque sensors, installed on a rigid and bulky frame, have been often used to measure the human intent for joints without direct interaction to the ground, but limit the system’s wearability. Also, inaccuracies may creep in easily due to the inevitable misalignment between the bionic joint center and human joint center, which may introduce undesired interaction force [15, 16]. Usually, it is challenging to directly measure the net ankle joint moment during walking overground with conventional force or torque sensors setup. The standard way to measure the net ankle joint moment uses a motion capture system, ground reaction force (GRF), and inverse dynamics (ID) calculations. However, there are two shortcomings of the standard approach. First, the setup is constrained to a lab environment, and not applicable for field testing. Second, the results from ID do not reveal how skeletal muscles perform during walking from a neuromuscular perspective. Therefore, a forward dynamics approach based on a neuromuscular model would be very instrumental when a motion capture system and GRF data are unavailable.

Surface electromyography (sEMG) measures electrical potentials during asynchronous muscle neurons firings, and its amplitude and frequency positively relate to muscle activation levels. Therefore, sEMG-derived signals can be used in a Hill-type neuromuscular model (HNM) or to train a machine learning approach (model-free) to predict volitional joint moment [17, 18] and angular position [19–21]. However, sEMG signals suffer from interference or cross-talking from the adjacent muscles, and an inability of measuring activations of deep-layer muscles [22, 23]. Alternatively, two-dimensional brightness mode (B-mode) ultrasound (US) imaging allows one to see the musculature of the targeted muscle *in vivo*. Due to its ability to directly visualize superficial and deep-layer muscles, US imaging may work as an alternative methodology to predict joint motion or motion intent. Potentially, US imaging overcomes the shortcomings of the sEMG measurements. Most frequently used architectural features from US images include pennation angle (PA) [24, 25], fascicle length (FL) [26, 27], muscle thickness (MT) [28, 29], and cross-sectional

area [30]. These features have been correlated with the joint kinetics and kinematics during isometric or isokinetic joint motion by using HNM-based or model-free approaches [25, 31–33].

Motivation also exists to use a dual-modal approach that combines the measurement from sEMG and US imaging. Potentially sEMG signals and US imaging provide complementary information, and the combination between them may 1) mitigate any cross-talking effect from neighboring sEMG signals and 2) lower US imaging-derived features' drift due to the accumulated errors from cyclic joint movement. Our recent studies have shown the advantages of using the dual-modal approach over uni-modal bio-signals (sEMG or US imaging) for ankle joint moment/motion prediction under isometric/dynamic dorsiflexion studies [21, 25, 27] and isometric plantarflexion study [34, 35]. Similarly, Dick *et al.* used both sEMG and US imaging to predict plantarflexion force during dynamic cycling tasks [32]. However, the use of the dual-modal bio-signals during more complex functional tasks, like walking across different speeds remains unexplored.

In this study, we investigated a dual-modal approach that takes both processed sEMG and MT from US imaging as inputs to a modified HNM, named sEMG-US imaging-driven HNM, to predict net ankle joint plantarflexion moment during the walking stance phase across multiple speeds. We hypothesize that 1) the proposed HNM will achieve a better net plantarflexion moment prediction accuracy than sEMG-driven and US imaging-driven HNMs, 2) the net plantarflexion moment prediction performance is more robust if data collected from multiple speeds are included in HNMs' calibration procedure.

In previous US imaging studies, visualized architectural features, such as PA and FL, require high-resolution US imaging, which can be significantly affected by a US transducer placement site on the muscle. To mitigate the requirement of high-resolution US imaging, US imaging-derived signals such as echogenicity [27, 36, 37], tissue displacement [38], and MT [29], are more preferable to correlate with muscle or joint mechanical functions. Because ankle plantarflexors: lateral and medial gastrocnemius and soleus muscles (LGS, MGS, and SOL) are not accessible in the same US image plane, this study chose to focus on LGS and SOL, which are in the same plane, and tracked their MT change during the walking experiments across multiple speeds. Therefore, the contributions of the paper are: 1) the use of US imaging-derived MT changes and sEMG-derived changes of LGS and SOL muscles as surrogate variables of muscle activations during walking, 2) development of a modified HNM that uses both sEMG and US imaging as inputs for single-speed modes and an inter-speed mode, and 3) evaluation of the sEMG-US imaging-driven HNM's robustness across multiple walking speeds.

Method

Hill-type Neuromuscular Model of Ankle Joint

Below, we propose a modified sEMG-US imaging-driven HNM to directly build a relationship between the joint net PF moment and sEMG-US imaging-derived surrogate signals of both LGS and SOL muscles. There are three sub-models involved in the HNM: (a) sEMG-US imaging-derived weighted muscle activation model, (b) muscle-tendon unit geometry model, and (c) muscle contraction dynamic model.

Weighted muscle activation model

The neural activation at t_k time instant $N_i(t_k)$, $i = 1, 2$, $k = 1, 2, 3, \dots$, for SOL and LGS muscles, respectively, considers the electromechanical delay (EMD), τ , between the onset of an sEMG signal and a muscle contraction and utilizes a second-order recursive filter and is defined as [39]

$$N_i(t_k) = \alpha_i u_i(t_{k-\tau}) - \beta_{1i} N_i(t_{k-1}) - \beta_{2i} N_i(t_{k-2}) \quad (1)$$

where EMD, τ , is usually between 30 ms and 120 ms. $u_i(t_k)$ represents the sEMG's linear envelope normalized to the value at maximum volitional contraction (MVC). The sEMG's linear envelope was derived after raw sEMG signals' band-pass filtering, full-wave rectification, and low-pass filtering. α_i , β_{1i} , and β_{2i} are coefficients that define the recursive filter's dynamics of each muscle [39], and the following set of constraints is employed to reach a positive stable solution, i.e.

$$\beta_{1i} = \gamma_{1i} + \gamma_{2i}, \beta_{2i} = \gamma_{1i} \cdot \gamma_{2i}, \alpha_i - \beta_{1i} - \beta_{2i} = 1 \quad (2)$$

where $|\gamma_{1i}| < 1$ and $|\gamma_{2i}| < 1$.

A nonlinear relationship between neural activation $N_i(t_k)$ and corresponding muscle activation $a_{1i}(t_k)$ is given as [39]

$$a_{1i} = \frac{e^{A_i N_i} - 1}{e^{A_i} - 1} \quad (3)$$

where A_i represents the nonlinear shape factor for each muscle, which is allowed to vary between -3 and 0, with $A_i = -3$ being a nonlinear and $A_i = 0$ being a linear relationship.

According to the reported results in [40–43], the MT change was found to correlate with the muscle contraction level or muscle activation through a linear function or piece-wise linear function. Therefore, in this work, the second part of the LGS or SOL muscle activation is calculated from the US imaging-derived MT change. The MT values of LGS and SOL muscles are denoted as $MT_i(t_k)$. According to the preliminary results in [44], there is a positive relationship between MT change and the targeted muscle contraction level during the walking stance phase. After taking normalization of the MT with respect to the lower bound (at rest state) and upper bound (at MVC) on each participant, the US imaging-derived muscle activation, $a_{2i}(t_k)$, is proposed as

$$a_{2i} = \frac{MT_i - MT_{i \min}}{MT_{i \max} - MT_{i \min}} \quad (4)$$

where $MT_{i \max}$ and $MT_{i \min}$ represent the constant subjective MT values when the LGS and SOL muscles are at MVC condition and rest condition, respectively. This normalization guarantees that the US imaging-derived muscle activations vary between 0 and 1.

By introducing an allocation gain between the sEMG- and US imaging-derived muscle activations, the synthesized/weighted muscle activation levels for LGS or

SOL muscle, $a_i(t_k)$, can be represented as

$$a_i = \delta_i a_{1i} + (1 - \delta_i) a_{2i} \quad (5)$$

where $\delta_i \in [0, 1]$ represents the muscle activation allocation gain for LGS ($i = 1$) and SOL ($i = 2$) muscles.

Muscle-tendon unit geometry model

Figure 1: **The muscle-tendon-unit (MTU) geometry model of the ankle joint plantarflexion function.** The ankle joint rotation center in the sagittal plane is denoted as O , and the proximal and distal osteotendinous junction points near the knee joint and heel are denoted as A and B . SOL and LGS muscles are referred as $i = 1, 2$.

As presented in Fig. 1, consider the ankle joint rotation center in the sagittal plane as O , the proximal and distal osteotendinous junction points of each muscle-tendon unit (MTU) near the knee joint and heel as A_i and B_i , and the angle between OA_i and OB_i as $q(t_k)$, then each MTU length, $l_{mt_i}(t_k)$, is represented as the distance between A_i and B_i , and is calculated as

$$l_{mt_i} = \sqrt{l_{OA_i}^2 + l_{OB_i}^2 - 2l_{OA_i}l_{OB_i}\cos(q)} \quad (6)$$

where l_{OA_i} and l_{OB_i} represent the distance of OA_i and OB_i obtained from OpenSim (National Institutes of Health for Biomedical Computation, Stanford, USA) [45], respectively. A generic OpenSim model (*gait2392*) was linearly scaled to each participant in OpenSim version 4.1 [45] per [46]. According to the law of sines, the moment arm of each MTU, $r_{mt_i}(t_k)$, is calculated as

$$r_{mt_i} = \frac{\partial l_{mt_i}(q)}{\partial (q)} = \frac{2l_{OA_i}l_{OB_i}\sin(q)}{l_{mt_i}}. \quad (7)$$

The MTU generates contraction force only when it is stretched, which indicates the current tendon length $l_{t_i}(t_k)$ is equal to or longer than the tendon slack length $l_{t_i}^{sk}$. From a more physiological perspective, the overall MTU length, $l_{mt_i}(t_k)$, could also be expressed as

$$l_{mt_i} = l_{t_i} + l_{m_i}\cos(\phi_i) \quad (8)$$

where $l_{t_i}(t_k)$ and $l_{m_i}(t_k)$ represent the current tendon length and muscle fascicle length for LGS and SOL muscles, respectively. $\phi_i(t_k)$ represents the pennation angle that changes with instantaneous $l_{m_i}(t_k)$. By assuming the individual muscle belly has a relatively small MT change and volume change [47, 48], $\phi_i(t_k)$ can be approximately calculated as

$$\phi_i \approx \arcsin\left(\frac{l_{m_i}^0 \sin \phi_i^0}{l_{m_i}}\right) \quad (9)$$

where the term ϕ_i^0 denotes the constant pennation angle when the muscle is at optimal fascicle length $l_{m_i}^0$. The work in [49, 50] has shown that the optimal fascicle length increases as muscle activation decreases. Due to this coupling, the following relationship between the muscle activation and corresponding optimal fascicle length is given as

$$l_{m_i}^0 = l_{m_{o_i}}^0 (\lambda(1 - a_i) + 1) \quad (10)$$

where λ is the rate of change in the optimal fascicle length, and it is selected as 0.15 [39]. $l_{m_{o_i}}^0$ is the optimal fascicle length at MVC, and $l_{m_i}^0(t_k)$ is the optimal fascicle length at time t_k and muscle activation $a_i(t_k)$.

From the preliminary results of plantarflexors' US imaging in [44], it is very challenging to capture the entire fascicle length $l_{m_i}(t_k)$ of LGS or SOL muscles by using the current US transducer with a small dimension (width of 38 mm). Therefore, the fascicle length parameters of either LGS or SOL muscles were not measured directly from the US images. Instead, an indirect calculation method was applied as detailed below. According to [51], the nonlinear nominal tendon force-tendon strain relationship is given as

$$F_{t_i}(\xi_i) = \begin{cases} 0, & \xi \leq 0 \\ 1480.3 F_i^{\max} \xi_i^2, & 0 < \xi < 0.0127 \\ (37.5 \xi_i - 0.2375) F_i^{\max}, & \xi \geq 0.0127 \end{cases} \quad (11)$$

where $\xi_i = \frac{l_{t_i}(t_k) - l_{t_i}^{s_k}}{l_{t_i}^{s_k}}$ represents the tendon strain and F_i^{\max} represents the muscle contraction force at MVC. By considering $F_{t_i}(\xi_i) = F_{mt_i}$, where F_{mt_i} is defined in (13), $l_{t_i}(t_k)$ can be numerically computed based on the Runge-Kutta-Fehlberg algorithm. By substituting (6) and (9) to (8), the muscle fascicle length $l_{m_i}(t_k)$ will be calculated, as well as the muscle fascicle velocity $v_{m_i}(t_k)$ by taking the time derivative of $l_{m_i}(t_k)$.

Muscle dynamic contraction model

In the sEMG-US imaging-driven HNM, the individual moment component produced by each muscle, $M_i(t_k)$, can be represented as

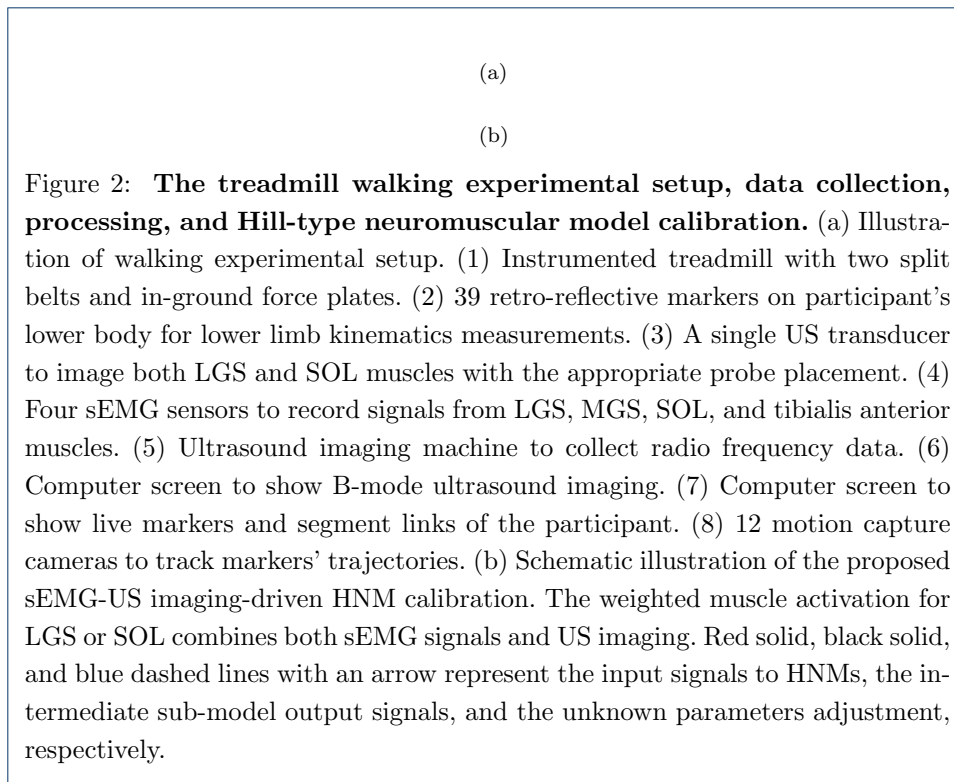
$$M_i = F_{mt_i} r_{mt_i} \quad (12)$$

where $r_{mt_i}(t_k)$ is defined in the above geometry model and $F_{mt_i}(t_k)$ denotes the corresponding contraction force generated on each MTU and is represented as

$$F_{mt_i} = (F_{ce_i} + F_{pe_i}) \cos(\phi_i) \quad (13)$$

where $\phi_i(t_k)$ represents the pennation angle defined above. $F_{ce_i}(t_k)$ and $F_{pe_i}(t_k)$ denote the corresponded forces generated by the parallelly located contractile element and the passive element, and can be calculated as

$$\begin{aligned} F_{ce_i} &= F_i^{\max} f_{l_i}(l_{m_i}) f_{v_i}(v_{m_i}) a_i \\ F_{pe_i} &= F_i^{\max} f_{p_i}(l_{m_i}) \end{aligned} \quad (14)$$



In (14), F_i^{\max} of the LGS and SOL muscles will be identified based on optimization algorithm in the HNM calibration procedures. $f_{l_i}(l_{m_i}(t_k))$, $f_{v_i}(v_{m_i}(t_k))$, and $f_{p_i}(l_{m_i}(t_k))$ denote the generic muscle contractile force-fascicle length, force-fascicle velocity, and passive elastic force-fascicle velocity curves. These curves were normalized to F_i^{\max} , optimal fascicle length $l_{m_i}^0$, and maximum fascicle contraction velocity $v_{m_i}^{\max}$. The explicit expressions of $f_{l_i}(l_{m_i}(t_k))$, $f_{v_i}(v_{m_i}(t_k))$, and $f_{p_i}(l_{m_i}(t_k))$ can be found in [25, 32, 52].

Experimental Protocol, Data Collection and Pre-processing

The study was approved by the Institutional Review Board (IRB) at North Carolina State University (IRB number: 20602). Ten young participants (7M/3F, age: 25.4 ± 3.1 years, height: 1.77 ± 0.10 m, mass: 78.0 ± 21.1 kg) without any neuromuscular or orthopedic disorders, were recruited in this study. Every participant got familiar with the experimental procedures and signed an informed consent form before participation.

Figure 2 (a) summarizes the experimental setup for the participants to perform static anatomical poses and dynamic gait trials (walking speeds changing from 0.50 m/s to 1.50 m/s), and Fig. 2 (b) presents the workflow of the data processing and sEMG-US imaging-driven HNM calibration procedures. The apparatus applied in the current study and data collection during dynamic walking trials are detailed in the supplementary materials. sEMG signals were band-pass filtered with the bandwidth between 20 Hz and 450 Hz, and then full-wave rectified and low-pass filtered with a cut-off frequency of 6 Hz. The resulting linear envelopes were normalized to the peak processed sEMG values obtained from all sets of dynamic gait trials

with different speeds. The US radio frequency data were converted to B-mode images through beamforming and logarithmic compression, and then a commercial US imaging processing toolbox *UltraTrack* [53] was applied to determine the temporal sequences of the LGS and SOL muscles' thickness based on the adaptive optical flow tracking algorithms. First, one region of interest (width by height: 336×400 pixels) that encompassed the LGS and SOL muscles was selected as the area between the superficial and deep aponeuroses. Then, 10 vertical lines were manually defined with evenly distributed distances in the LGS's region and SOL's region on the first US imaging frame for each recorded waking trial, as shown in Fig. 2 (b). Key-frame correction [53] was applied to minimize the time-related drift of MT's cyclical pattern over multiple gait cycles, where the key frames were selected to be at heel-strike and toe-off time points. After each correction, the new key frames' vertical lines positions were determined by applying an affine transformation to the key-frame before it. Finally, the temporal sequence of the mean value of those 10 vertical lines' lengths from LGS and SOL muscles were calculated for LGS's MT and SOL's MT, respectively. The MT signals were then low-pass filtered with a cut-off frequency of 30 Hz.

Before data collection, participants practiced dynamic walking steadily with all sensing devices attached to the lower extremities on the treadmill for at least 30 seconds for each speed. The duration of each walking trial was set as 2 minutes, and data from the middle 20 seconds were collected for analysis. In the current study, there were five different walking speeds, 0.50 m/s, 0.75 m/s, 1.00 m/s, 1.25 m/s, and 1.50 m/s, and the order was selected randomly for each participant. The participants were provided with at least 2 minutes for rest between two successive dynamic walking trials to avoid muscle fatigue.

Data Post-processing

HNM model calibration

To determine the values for a set of parameters, including the shape factor A_i , the tendon slack length $l_{t_i}^{sk}$, the muscle contraction force at MVC F_i^{max} , and the muscle activation allocation gain δ_i , the HNM model calibration was performed with the initial parameters obtained from the literature [54]. The summarized calibration process of the sEMG-US imaging-driven HNM is presented in Fig. 2 (b). During calibration, the parameters were subsequently adjusted within the predefined boundaries, which ensured the muscle-tendon unit always operated within the physiological range [39]. Other HNM parameters, like muscle-tendon unit length l_{mt_i} , optimal muscle fascicle length $l_{mo_i}^0$, and optimal pennation angle ϕ_i^0 were assigned using OpenSim and the scaling method as references. The Levenberg-Marquardt algorithm was applied to solve the nonlinear least-squares optimization problem until the following objective function was minimized during the calibration

$$E_{obj} = \frac{1}{N} \sum_{j=1}^N \left(\left(\sum_{i=1}^2 M_i(j) \right) - M_w(j) \right)^2 \quad (15)$$

where $\sum_{i=1}^2 M_i(j)$ represents the net PF moment estimation from both LGS and SOL muscles during stance phase at time instant j , $M_w(j)$ represents the net PF

moment measurement from ID at time instant j , and N represents the length of the data used for the calibration.

It should be noted that the HNM calibration is subjective, and for each participant, the calibration procedure was repeated for both single-speed modes and inter-speed mode. In the current study, single-speed modes are defined as the HNM calibration only with data collected from one single speed (five single-speed modes here), while the inter-speed mode is defined as the HNM calibration with all data collected from five different speeds (one inter-speed mode here). In HNM calibration, collected data, including ankle joint's kinematics, kinetics, sEMG signals, and US imaging from the stance phase of 10 steady gait cycles, were used to minimize the objective function in (15). For the single-speed modes, the 10 steady gait cycles were all from one speed, while for the inter-speed mode, the 10 gait cycles were composed of two steady cycles from each of five speeds. Similarly, by manually setting the muscle activation allocation gain δ_i to be 1 and 0, we could also conduct the calibration procedures of the sEMG-driven and US imaging-driven HNMs. After the HNM calibration with different modes, new data sets (five gait cycles not involved in the calibration procedures) from walking trials at different speeds were used as input of the calibrated HNMs to predict net PF moment. The prediction results were evaluated through the comparison to the measured net PF moment from ID.

Statistical Analysis

The validation procedures comprised three tests to assess the sEMG-US imaging-driven, sEMG-driven, and US imaging-driven HNMs' calibration and prediction abilities of the net ankle joint PF moment during the stance phase. In each type of HNM test, the root mean square error ($RMSE$), $RMSE$ normalized to individual net PF moment at MVC ($N - RMSE$), $RMSE$ normalized to individual body mass ($BM - RMSE$), and coefficient of determination (R^2) values between the calibrated/predicted net PF moment and ID-calculated net PF moment were calculated to evaluate the calibration/prediction performance.

Shapiro-Wilk parametric hypothesis test was used to determine the normality of the corresponding $N - RMSE$, $BM - RMSE$, and R^2 values of each calibration step under the single-speed modes and inter-speed mode, and each prediction step. According to the results of the Shapiro-Wilk test, two-way repeated-measure analysis of variance (ANOVA) or Friedman's tests followed by a Tukey's honestly significant difference tests (Tukey's HSD) was applied to evaluate the effect of HNMs' category and walking speed on different evaluation criteria, including $N - RMSE$, $BM - RMSE$, and R^2 values, during both calibration and prediction procedures. The significant difference level was chosen as $p < 0.05$ for all statistical tests. Effect sizes were reported as η_p^2 and Cohen's d for main effects from ANOVA or Friedman's tests and pairwise comparisons from Tukey's HSD, respectively.

Results

Ankle joint kinematics and kinetics, and plantarflexors neuromuscular features

The treadmill walking speed's effect on human ankle joint kinematics, kinematics, and lower extremities' muscles activities has been extensively investigated and discussed in a recent study [55], but without results related to the architectural change

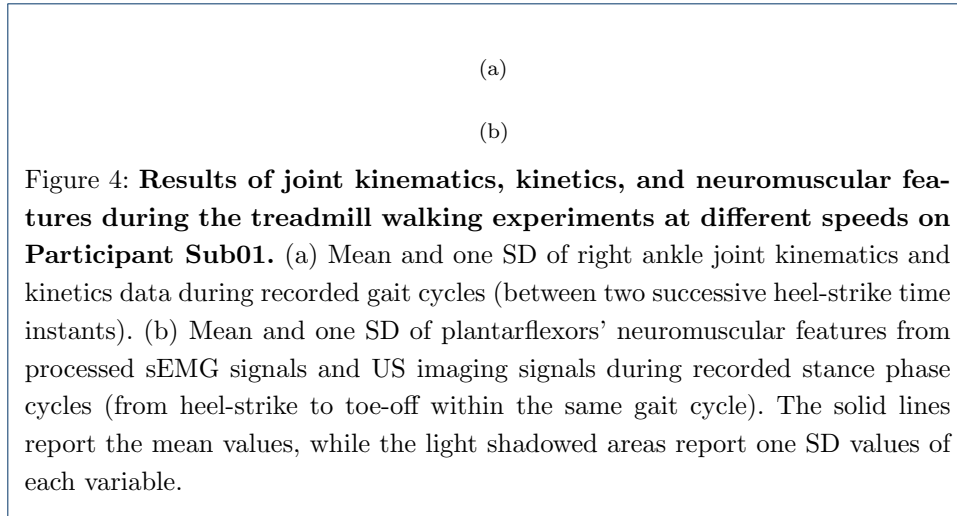
of those muscles. In this study, the time sequences of both LGS and SOL's muscle thickness during the recorded walking duration were extracted by using *UltraTrack*. Take the SOL muscle of Participant Sub08 as an example, Fig. 3 shows the MT tracking results throughout the 20 s walking duration at each walking speed. The red solid and blue dashed curves represent the MT change of the SOL muscle with and without key-frame correction, respectively. The results demonstrate that the key-frame correction could significantly reduce the time-related drift, which is due to the tracking error accumulation along with the walking duration. The reported results here are consistent with the studies mentioned in [53].

Figure 3: **SOL muscle thickness tracking results by using *UltraTrack* at different walking speeds on Participant Sub08.** Each subplot represents the tracking results during the recorded 20 s experiments under each walking speed, and the red solid and blue dashed lines represent the results with and without key-frame correction, respectively.

The continuous results of the ankle joint kinematics, kinetics, and neuromuscular features throughout the recorded walking duration were segmented and analyzed into multiple gait cycles. Fig. 4 (a) shows the mean and one standard deviation (SD) of the right ankle joint angular position, velocity, and net moment changes across all gait cycles at multiple speeds on Sub01 (data from other participants can be found in the supplementary materials), where 0% represents the time instant when the heel-strike occurred. By comparing the ankle joint moment calculated from ID, the averaged peak net PF moment across all walking gait cycles within each walking trial monotonically increased with the increase of walking speeds on each participant, indicating more power was needed for faster walking speed. Fig. 4 (b) shows the processed neuromuscular features from US imaging and sEMG signals of LGS and SOL muscles during the stance phase across multiple gait cycles under each speed condition on Sub01. The upper two rows present the LGS and SOL MT changes during the stance phase, while the lower two rows present the muscle's low-pass filtered sEMG changes. The results show small variations of MT and sEMG for both LGS and SOL muscles at heel-strike across all walking speeds, but relatively high variations of sEMG for both LGS and SOL muscles at toe-off, where the sEMG signals increase with increased walking speed. For all five walking speeds, we observe that MT of LGS or SOL muscle is almost identical at heel-strike and toe-off, however, the processed sEMG signals of LGS or SOL muscle show higher value at toe-off than at heel-strike. By comparing the shadowed areas of the same feature across speeds, we observed that features' deviations are higher at a slower speed, like 0.50 m/s, than those at higher speeds. This implies that keeping a steady muscle contraction pattern at a slower speed is more difficult than at a higher speed.

Correlation analysis results

Overall, in Fig. 4 (b), both temporal MT and sEMG signals from LGS and SOL muscles show a fairly strong correlation with the net ankle joint PF moment calculated from ID. The mean and one SD values of correlation coefficients between



each neuromuscular feature and net PF moment are listed in Table 1. Each data cell represents the summarized correlation result of an individual neuromuscular feature at individual walking speed across all stance phase cycles and participants. The results show that a positive relationship exists between the processed LGS or SOL's sEMG signal and net PF moment, and between the LGS or SOL's MT and net PF moment. All the mean values of correlation coefficients are higher than 0.8 except for the SOL's sEMG signal at 1.50 m/s walking speed. From the results of a two-way repeated-measure ANOVA, we did not observe a significant difference in the correlation coefficient values among the four neuromuscular features ($p = 0.201$) or among the walking speed ($p = 0.112$), which indicates the MT and sEMG signals might have comparable capabilities to predict net PF moment across speeds.

Results of HNM calibration and net PF moment prediction

Figure 5 presents the representative results of HNMs calibrations on Sub05 with data collected from each individual walking speed, where each solid centered line and the shadowed area represent the mean and one SD values of the measured and calibrated net ankle joint PF moment, and each curve is composed of 10 stance cycles at each walking speed. For this participant, the mean calibration *RMSE* values are 8.70 N·m, 9.10 N·m, and 7.90 N·m by using sEMG-, US imaging-, and sEMG-US imaging-driven HNMs under walking speed of 0.50 m/s, respectively. Results from other walking speeds also showed that the sEMG-US imaging-driven HNM could effectively reduce the calibration *RMSE* under either single-speed modes or

Table 1: Correlation coefficients (mean \pm SD) between each neuromuscular feature and the net PF moment across all stance phase cycles and ten participants at each walking speed.

		Neuromuscular features			
		LGS sEMG	SOL sEMG	LGS MT	SOL MT
Speed [m/s]	0.50	0.886 (0.019)	0.876 (0.086)	0.857 (0.052)	0.867 (0.053)
	0.75	0.890 (0.058)	0.905 (0.054)	0.842 (0.024)	0.865 (0.032)
	1.00	0.892 (0.066)	0.896 (0.056)	0.883 (0.063)	0.892 (0.056)
	1.25	0.835 (0.096)	0.857 (0.076)	0.840 (0.034)	0.833 (0.033)
	1.50	0.801 (0.124)	0.785 (0.081)	0.847 (0.018)	0.844 (0.022)

(a)
(b)
(c)
(d)
(e)

Figure 5: Calibration results by using three HNM categories on Participant Sub05 under single-speed modes. The calibration performance by using sEMG-, US imaging-, and sEMG-US imaging-driven HNMs under 5 single-speed modes on Sub05. The red lines and light shadowed areas represent the mean and SD of the net PF moment from the ID calculation, the blue, green, black lines and light shadowed areas represent the mean and SD of the net PF moment from calibrations by using sEMG-driven HNM, US imaging-driven HNM, and sEMG-US imaging-driven HNM, respectively. (a)-(e) represent the results at each walking speed from 0.50 m/s to 1.50 m/s.

Figure 6: Calibration performance across all participants by using three HNM categories. The mean and SD of $BM - RMSE$, $N - RMSE$, and R^2 values across all participants under both single-speed modes and inter-speed mode are displayed in upper, middle, and lower plots, respectively, during calibration procedures. Blue, red, and yellow bars represent the results by using sEMG-, US imaging-, and sEMG-US imaging-driven HNMs, respectively.

inter-speed mode. To quantitatively evaluate the calibration performance by using different HNM categories and under different speed modes, the mean $RMSE$ and R^2 values between the benchmark moment values from ID and calibrated moment values on each participant are summarized in Table 2.

Overall, the calibration $RMSE/R^2$ values by using the sEMG-US imaging-driven HNM are lower/higher than those by using the sEMG-driven and US imaging-driven HNMs, respectively, for both single-speed modes and inter-speed mode on all participants. Additionally, 97.5 % of R^2 values are higher than 0.80, which indicates a strong linear correlation between the calibrated and ID-calculated net PF moment values. After calculating the $N - RMSE$ and $BM - RMSE$ values, the summarized calibration performance across all participants under both single-speed modes and inter-speed mode is presented in Fig. 6. Shapiro-Wilk tests show that all $N - RMSE$, $BM - RMSE$, and R^2 values under the single-speed modes and inter-speed mode in both calibration and prediction are normally distributed. In calibration, results across participants from the two-way ANOVA show $BM - RMSE$ values systematically changed in response to changes in speed (main effect, $p < 0.001$, $n_p^2 = 0.268$) and applied HNMs (main effect, $p < 0.001$, $n_p^2 = 0.162$). $N - RMSE$ values systematically changed in response to changes in speed (main effect, $p <$

Table 2: Calibration results with three HNM categories in both single-speed modes and inter-speed mode on each participant. (*RMSE* unit: N·m)

		Single-speed modes					
		0.50 m/s		0.75 m/s		1.00 m/s	
Subject	HNMs	<i>RMSE</i>	<i>R</i> ²	<i>RMSE</i>	<i>R</i> ²	<i>RMSE</i>	<i>R</i> ²
Sub01	sEMG	12.16	0.954	11.28	0.956	12.75	0.954
	US imaging	14.49	0.921	14.62	0.926	12.94	0.951
	sEMG-US imaging	11.79	0.965	10.25	0.964	11.77	0.960
Sub02	sEMG	5.96	0.932	6.93	0.936	7.70	0.934
	US imaging	5.91	0.932	6.44	0.943	7.07	0.945
	sEMG-US imaging	4.94	0.953	5.10	0.964	6.91	0.947
Sub03	sEMG	9.86	0.924	8.38	0.964	11.28	0.949
	US imaging	13.68	0.857	11.17	0.937	12.29	0.940
	sEMG-US imaging	8.33	0.946	6.49	0.979	9.81	0.962
Sub04	sEMG	12.04	0.820	17.14	0.842	13.79	0.904
	US imaging	16.60	0.661	20.49	0.771	16.38	0.865
	sEMG-US imaging	11.64	0.834	16.89	0.847	13.48	0.908
Sub05	sEMG	8.70	0.903	9.43	0.904	9.01	0.921
	US imaging	9.10	0.894	9.77	0.897	9.54	0.911
	sEMG-US imaging	7.90	0.920	8.96	0.913	8.97	0.921
Sub06	sEMG	6.36	0.963	6.15	0.974	9.35	0.953
	US imaging	7.08	0.954	12.42	0.897	18.34	0.823
	sEMG-US imaging	5.53	0.972	6.02	0.976	9.28	0.954
Sub07	sEMG	5.76	0.923	6.75	0.921	6.84	0.949
	US imaging	6.22	0.911	8.34	0.879	7.31	0.942
	sEMG-US imaging	5.46	0.932	6.48	0.927	6.67	0.951
Sub08	sEMG	4.98	0.973	6.64	0.957	9.20	0.936
	US imaging	4.97	0.973	6.97	0.953	8.34	0.946
	sEMG-US imaging	4.61	0.977	6.35	0.961	8.24	0.948
Sub09	sEMG	7.37	0.926	8.65	0.919	7.76	0.941
	US imaging	8.99	0.894	9.55	0.901	8.13	0.936
	sEMG-US imaging	7.22	0.929	8.27	0.926	7.24	0.949
Sub10	sEMG	9.31	0.935	7.27	0.973	12.24	0.940
	US imaging	13.85	0.856	11.97	0.927	12.56	0.937
	sEMG-US imaging	8.25	0.949	5.78	0.983	9.72	0.962
		Single-speed modes				Inter-speed mode	
		1.25 m/s		1.50 m/s		All speeds	
Subject	HNMs	<i>RMSE</i>	<i>R</i> ²	<i>RMSE</i>	<i>R</i> ²	<i>RMSE</i>	<i>R</i> ²
Sub01	sEMG	13.40	0.955	14.59	0.953	14.42	0.936
	US imaging	13.85	0.952	13.38	0.960	18.79	0.893
	sEMG-US imaging	12.61	0.960	12.76	0.964	12.95	0.949
Sub02	sEMG	13.47	0.823	11.29	0.874	10.62	0.862
	US imaging	16.86	0.724	13.76	0.816	12.28	0.818
	sEMG-US imaging	13.41	0.822	8.79	0.922	10.01	0.877
Sub03	sEMG	11.55	0.950	12.07	0.946	13.53	0.924
	US imaging	11.62	0.950	13.01	0.938	16.19	0.916
	sEMG-US imaging	9.38	0.967	11.30	0.952	11.38	0.951
Sub04	sEMG	14.91	0.893	14.89	0.913	17.14	0.848
	US imaging	17.26	0.857	15.13	0.911	23.52	0.723
	sEMG-US imaging	14.87	0.894	14.86	0.914	17.12	0.849
Sub05	sEMG	6.79	0.963	8.15	0.954	10.60	0.892
	US imaging	6.87	0.961	8.51	0.949	12.97	0.840
	sEMG-US imaging	6.67	0.964	8.08	0.954	10.48	0.895
Sub06	sEMG	8.74	0.964	18.06	0.884	13.13	0.905
	US imaging	13.54	0.915	15.99	0.908	17.32	0.832
	sEMG-US imaging	8.37	0.967	13.91	0.931	11.76	0.922
Sub07	sEMG	7.66	0.941	10.59	0.898	9.46	0.890
	US imaging	7.38	0.946	9.37	0.920	10.41	0.868
	sEMG-US imaging	7.04	0.951	9.02	0.927	8.64	0.909
Sub08	sEMG	11.74	0.912	14.98	0.864	14.98	0.864
	US imaging	10.82	0.925	14.27	0.877	14.27	0.877
	sEMG-US imaging	10.44	0.931	13.76	0.886	13.76	0.886
Sub09	sEMG	7.55	0.925	8.02	0.954	10.58	0.929
	US imaging	9.64	0.878	8.28	0.923	14.38	0.870
	sEMG-US imaging	6.87	0.955	7.92	0.955	10.08	0.933
Sub10	sEMG	12.10	0.946	10.85	0.956	13.14	0.939
	US imaging	12.89	0.939	11.86	0.948	17.26	0.906
	sEMG-US imaging	10.19	0.962	10.08	0.962	12.37	0.960

0.001, $n_p^2 = 0.089$) and applied HNMs (main effect, $p < 0.001$, $n_p^2 = 0.193$). R^2 values were significantly affected by speed (main effect, $p < 0.001$, $n_p^2 = 0.153$) and applied HNMs (main effect, $p < 0.001$, $n_p^2 = 0.186$). However, there is no evidence of an interaction effect of the speed and HNM on $BM - RMSE$ values ($p = 0.679$), $N - RMSE$ values ($p = 0.948$), and R^2 values ($p = 0.279$), respectively.

To verify the net PF moment prediction performance of the proposed sEMG-US imaging-driven HNM and compare the new HNM to both sEMG- and US imaging-driven HNMs, the three calibrated HNM categories, shown in Fig. 6, were applied to walking scenarios of five different speeds. Similarly, $BM - RMSE$, $N - RMSE$, and R^2 values between the predicted and ID-calculated net PF moments were evaluated and compared. Due to the space limitation, the detailed $RMSE$ and R^2 values at each walking speed on individual participant in prediction can be found in the supplementary materials. The summarized results in Fig. 7 show the mean and one SD of $BM - RMSE$, $N - RMSE$, and R^2 values in prediction at each of five speeds by applying three HNM categories. The subplots from the first column to the fifth column represent the applied calibrated HNMs were from five single-speed modes, while the subplots from the sixth column represent the inter-speed mode. In each subplot, the x -axis labels represent the prediction scenarios at five different speeds. Table 3 summaries the mean values of $BM - RMSE$, $N - RMSE$, and R^2 in the prediction by using the proposed sEMG-US imaging-driven HNM, where the bold numbers represent the cases that the calibration speed mode is the same as the prediction speed scenario, which always results in the lowest $RMSE$ and highest R^2 values. From Fig. 7 and Table 3, we observed that $BM - RMSE$, $N - RMSE$, and R^2 values are optimal when the applied calibrated single-speed mode is close to the current prediction speed scenario, regardless of HNM categories. Furthermore, the calibrated inter-speed mode can effectively constrain the $BM - RMSE$, $N - RMSE$, and R^2 values within a small variation range among all prediction speed scenarios, regardless of HNM categories.

The results of two-way repeated-measure ANOVA show that in prediction $BM - RMSE$ values are significantly affected by the calibration speed mode (main effect, $p < 0.001$, $\eta_p^2 = 0.104$) and applied HNM category (main effect, $p < 0.001$, $\eta_p^2 = 0.141$), $N - RMSE$ values are significantly affected by the calibration speed mode (main effect, $p < 0.001$, $\eta_p^2 = 0.101$) and applied HNM category (main effect, $p < 0.001$, $\eta_p^2 = 0.164$), and also R^2 values are significantly affected by the calibration speed mode (main effect, $p < 0.001$, $\eta_p^2 = 0.103$) and applied HNM category (main effect, $p < 0.001$, $\eta_p^2 = 0.164$). The pairwise comparisons show that across all prediction scenarios with every speed mode calibration, the proposed sEMG-US imaging-derived HNM could significantly reduce the $BM - RMSE$ values by 14.49% ($p = 0.029$, $d = -0.348$) and 36.94% ($p < 0.001$, $d = -0.930$), significantly reduce the $N - RMSE$ values by 14.58% ($p = 0.012$, $d = -0.389$) and 36.79% ($p < 0.001$, $d = -1.021$), and increase the R^2 values by 9.71% ($p = 0.023$, $d = 0.713$) and 17.86% ($p < 0.001$, $d = 1.010$) compared to sEMG-driven and US imaging-driven HNMs, respectively. Furthermore, the pairwise comparisons also show that across all prediction scenarios with every HNM category, the inter-speed mode calibration could reduce the $BM - RMSE$ values by 38.74% ($p < 0.001$, $d = -0.922$), 18.86% ($p = 0.180$, $d = -0.590$), 8.87% ($p = 0.826$, $d = -0.237$), 9.84% ($p = 0.785$,

Figure 7: **Prediction performance across all participants by using three HNM categories.** The mean and SD of $BM - RMSE$, $N - RMSE$, and R^2 values across all participants under both single-speed modes and inter-speed model are displayed in upper, middle, and lower row plots, respectively. Blue, red, and yellow bars represent the prediction results by using sEMG-, US imaging-, and sEMG-US imaging-driven HNMs, respectively. Column subplots from left to right represent that these applied HNMs were calibrated under single-speed modes (0.50 m/s, 0.75 m/s, 1.00 m/s, 1.25 m/s, and 1.50 m/s) and the inter-speed mode.

Table 3: Metrics of $BM - RMSE$, $N - RMSE$, and R^2 mean values of the net PF moment prediction across all participants by using the proposed sEMG-US imaging-driven HNM. The diagonal elements with bold numbers represent the situations that the calibration speed mode is the same as the prediction speed scenario. ($BM - RMSE$ unit: N·m/kg, $N - RMSE$ unit: %)

$BM - RMSE$		Prediction scenario (m/s)				
		0.50	0.75	1.00	1.25	1.50
Calibration	0.50 m/s	0.119	0.154	0.221	0.276	0.333
	0.75 m/s	0.151	0.121	0.171	0.221	0.284
	1.00 m/s	0.216	0.162	0.127	0.176	0.275
	1.25 m/s	0.254	0.182	0.159	0.148	0.214
	1.50 m/s	0.271	0.226	0.215	0.214	0.155
	Inter-speed	0.161	0.126	0.150	0.163	0.217
$N - RMSE$						
Calibration	0.50 m/s	8.36	9.78	12.72	14.66	16.35
	0.75 m/s	10.75	7.75	9.75	11.71	14.04
	1.00 m/s	15.29	10.29	7.39	9.39	13.54
	1.25 m/s	17.97	11.52	9.01	7.89	10.87
	1.50 m/s	19.22	14.33	12.36	11.44	7.71
	Inter-speed	11.40	8.01	8.60	8.65	10.84
R^2						
Calibration	0.50 m/s	0.909	0.895	0.876	0.854	0.794
	0.75 m/s	0.863	0.943	0.930	0.908	0.845
	1.00 m/s	0.838	0.933	0.948	0.920	0.855
	1.25 m/s	0.809	0.912	0.928	0.940	0.904
	1.50 m/s	0.769	0.855	0.877	0.899	0.946
	Inter-speed	0.881	0.933	0.943	0.935	0.899

$d = -0.299$), and 26.57% ($p = 0.004$, $d = -0.836$), reduce the $N - RMSE$ values by 35.73% ($p < 0.001$, $d = -1.002$), 17.20% ($p = 0.201$, $d = -0.403$), 9.11% ($p = 0.881$, $d = -0.254$), 11.44% ($p = 0.715$, $d = -0.326$), and 28.08% ($p < 0.001$, $d = -0.817$), and increase the R^2 values by 16.76% ($p < 0.001$, $d = 0.810$), 5.33% ($p = 0.307$, $d = 0.342$), 0.40% ($p = 0.896$, $d = 0.044$), 0.31% ($p = 0.921$, $d = 0.033$), and 6.51% ($p = 0.127$, $d = 0.487$) compared to single-speed mode calibration at 0.50 m/s, 0.75 m/s, 1.00 m/s, 1.25 m/s, and 1.50 m/s, respectively.

Discussions

For the first time, this study investigated net ankle joint PF moment continuous prediction during the walking stance phase based on an HNM approach that combines both sEMG-induced and US imaging-induced muscle activation components. We defined this approach as sEMG-US imaging-driven HNM for the net PF moment prediction. The modified HNM was validated with quasi-periodic data, including

sEMG signals and US imaging-derived MT from plantarflexors, ankle joint kinematics, and kinetics measurements from multiple treadmill walking stance phases gait cycles at five different speeds. We focused on two plantarflexor muscles, e.g., LGS and SOL, when characterizing the PF function during walking. The basic objective was to establish a modified HNM for either LGS or SOL muscles, including (1) a weighted muscle activation model component, (2) a muscle-tendon unit geometry model component, and (3) a muscle dynamic contraction model component. This study also investigated the effects of HNM categories (sEMG-, US imaging-, and sEMG-US imaging-driven) and calibration speed modes (single-speed modes and inter-speed mode) on the net PF moment prediction performance during the walking stance phase. The ID-calculated net PF moment worked as the benchmark in both calibration and prediction. The results support our hypothesis that compared to sEMG-driven and US imaging-driven HNMs, the sEMG-US imaging-driven HNM accurately predicts the net PF moment. Further, the HNMs, when calibrated with the inter-speed mode, robustly predict the net PF moment.

The evaluation of the proposed HNMs' calibration and prediction performance was based on three criteria: $BM - RMSE$, $N - RMSE$, and R^2 . In general, as reported in [56], the results were considered excellent if the $N - RMSE$ values were smaller than 15%. For the calibration, the results in Fig. 5 presented a good calibration performance by using each of three HNMs on Sub05. Furthermore, from results across participants shown in Fig. 6, we observed that the mean $N - RMSE$ values were all less than 10.92% regardless of the calibration speed modes and applied HNM categories. Primarily they were less than 8.30% irrespective of the calibration speed modes when applying the proposed sEMG-US imaging-driven HNM. For the prediction, as shown in Fig. 7 and Table 3, by applying the inter-speed mode calibrated sEMG-US imaging-driven HNM, the $N - RMSE$ mean values were all less than 11.40% throughout those five walking speeds scenarios, which validated the prediction results were all excellent. Therefore, both calibration and prediction results present consistent findings that the $N - RMSE$ values can be constrained within a satisfactorily small region by using the proposed sEMG-US imaging-driven HNM with the inter-speed mode calibration.

The superior net PF torque prediction of the sEMG-US imaging-driven HNM can be mainly due to the reason that the fused signals capture complementary mechanical and neural aspects of the muscle contraction [25]. Specifically, sEMG signals measure electric potentials generated by muscle motor units. The amplitude and density of sEMG signals linearly correlate with the number of firing neurons, which offers a physical measurement of the microphysiological response [57]. US imaging directly visualizes muscle change at the macrophysiological performance [58], when the same group of neural motor units is activated. Thus, sEMG features and US imaging features provide information from electrical and mechanical aspects, respectively, in response to the same physiological stimulus.

As a preliminary study of the sEMG-US imaging-driven HNM for walking on a treadmill across multiple speeds, the results are promising and can help overcome the challenges of joint motion intent detection in volitional control of assistive devices. However, there are still some limitations in the current study. First of all, only a few US imaging-derived parameters, MT from both LGS and SOL, measured muscle activation levels indirectly (a macrophysiological perspective). Other

US-derived parameters, like FL and PA [21, 25, 27, 35], of the MTU geometry model may further enrich the neuromuscular model. A potential difficulty here is the inability to capture a larger region of interest that contains entire muscle fascicles, mainly due to the small dimension of our US transducer. Another difficulty is to continuously track the muscle fascicles of the plantarflexors within the visualized region of interest during dynamic tasks, like walking. If always visualized, more geometry parameters from US imaging signals will likely further improve the HNM accuracy. Second, the US imaging-derived muscle activation was defined as a normalization function in (4). We also assumed a linear monotonic relationship between the MT of LGS or SOL and net PF moment change during the stance phase in Table 1. However, in [29, 59], it was observed that despite an increase in MT of the LGS and SOL muscles during the stance phase, their muscle activations decreased in the last 10% to 20% of the stance phase. Also, in fast walking, MT of SOL was observed to decrease in the first 10% of stance, while the muscle activation increased. The above inconsistency may result from the difference in experimental setup, sEMG sensor or US transducer placement on the targeted muscles, MT tracking approach from US imaging signals, etc. In future work, a further comparison will be conducted to evaluate the muscle geometry parameters change and sEMG signals change during the same walking tasks. As detailed in the pre-processing data section, a key-frame correction [53] was applied to reduce the gait cycle-related drift of MT tracking results significantly. However, a subjective error in the manual operation is inevitable. Therefore, it was not practical to altogether remove the gait cycle-related drift of US imaging-derived MT. This work has extended the preliminary results of voluntary isometric ankle PF studies [34, 35] to dynamic walking studies on non-disabled participants. Further experiments on patients with impaired plantarflexors are needed to verify the practicability of the proposed sEMG-US imaging-driven HNM for net ankle joint PF moment prediction. We also observed that the calibrated HNM with the inter-speed mode increased the net PF moment prediction robustness across different speed scenarios. The development of inter-speed HNM modeling is crucial because it will potentially allow a consistently accurate prediction performance of the net PF moment across multiple walking speeds. Furthermore, it will enable predicting and analyzing the dynamics of a more extensive set of walking speeds than was possible with a single-speed mode, resulting in a deeper understanding of the neuromuscular dynamics during the human walking stance phase. Finally, it may open up to the development of robust neuromuscular human-machine interfaces for the simultaneous and proportional control of wearable assistive devices such as powered orthoses and prostheses under different walking speeds.

Conclusion

This paper investigated the feasibility of an sEMG-US imaging-driven HNM to predict net ankle joint PF moment during the stance phase across multiple walking speeds. The results showed that on average, the net PF moment prediction *RMSE*, normalized to peak net PF moment/body mass, was significantly reduced when using the sEMG-US imaging-driven HNM, compared to sEMG-driven and US imaging-driven HNMs. The results also showed that the calibrated HNM with the

inter-speed mode were more robust for net PF moment prediction at different speed scenarios than HNMs with single-speed modes. The improved net ankle joint PF moment prediction during the dynamic walking tasks at different speeds could potentially lead to improved volitional control of assistive devices with more advanced and intelligent algorithms.

List of Abbreviations

GRF	ground reaction force
ID	inverse dynamics
HNM	Hill-type neuromuscular model
EMG	electromyography
sEMG	surface electromyography
PA	pennation angle
FL	fascicle length
MT	muscle thickness
MGS	medial gastrocnemius
LGS	lateral gastrocnemius
SOL	soleus
PF	plantarflexion
EMD	electromechanical delay
MVC	maximum volitional contraction
MTU	muscle-tendon unit
IRB	institutional Review Board
B-mode	brightness mode
ANOVA	analysis of variance
HSD	honestly significant difference test
RMSE	root mean square error
N-RMSE	root mean square error normalized to peak value
BM-RMSE	root mean square error normalized to body mass
η_p^2	Effect Size
SD	standard deviation
R	correlation coefficient
R^2	coefficient of determination
d	Cohen's d
US	ultrasound

Declarations

Ethics approval and consent to participate

The study was conducted according to the guidelines of the Declaration of Helsinki, and all experiments were approved by the Institutional Review Board of North Carolina State University (protocol number 20602 and date of approval 02/10/2020). Participants provided written and informed consent.

Consent for publication

Participants provided written and informed consent for publication.

Availability of data and materials

The datasets used and/or analyzed during the current study are available from the corresponding author on reasonable request.

Competing interests

The authors declare that they have no competing interests.

Funding

This research was funded by NSF Career Award grant number 2002261.

Author's contributions

QZ, JRF, and NS conceived and designed the experiments. QZ led the experimental setup, data collection, and data processing, analyzed and interpreted data, generated figures, and wrote the manuscript. NF collaborated with the experimental setup, processed ultrasound imaging data, and revised the manuscript. JRF provided technical support of using UltraTrack to process ultrasound imaging data and revised the manuscript. NS was the principal investigator, led the project, interpreted data, and revised the manuscript. All authors read and approved the final manuscript.

Acknowledgements

The authors would like to thank Alison Mayers and Mayank Singh for their help in experiments' conduction and data collection. We would also like to thank all participants for their involvement in the study.

Author details

¹Joint Department of Biomedical Engineering at the University of North Carolina-Chapel Hill and North Carolina State University, 1840 Entrepreneur Dr., 27695 Raleigh, NC, USA. ²Joint Department of Biomedical Engineering at the University of North Carolina-Chapel Hill and North Carolina State University, 333 S Columbia St., 27514 Chapel Hill, NC, USA.

References

1. Tzu-wei, P.H., Shorter, K.A., Adamczyk, P.G., Kuo, A.D.: Mechanical and energetic consequences of reduced ankle plantar-flexion in human walking. *J. Exp. Biol.* **218**(22), 3541–3550 (2015)
2. Iezzoni, L.I., McCarthy, E.P., Davis, R.B., Siebens, H.: Mobility difficulties are not only a problem of old age. *J. Gen. Intern. Med.* **16**(4), 235–243 (2001)
3. Takahashi, K.Z., Lewek, M.D., Sawicki, G.S.: A neuromechanics-based powered ankle exoskeleton to assist walking post-stroke: a feasibility study. *J. NeuroEngineering Rehabil.* **12**(1), 23 (2015)
4. Tamburella, F., Tagliamonte, N., Pisotta, I., Masciullo, M., Arquilla, M., Van Asseldonk, E., van Der Kooij, H., Wu, A., Dzeladini, F., Ijspeert, A., *et al.*: Neuromuscular controller embedded in a powered ankle exoskeleton: Effects on gait, clinical features and subjective perspective of incomplete spinal cord injured subjects. *IEEE Trans. Neural Syst. Rehabil. Eng.* **28**(5), 1157–1167 (2020)
5. Young, A.J., Ferris, D.P.: State of the art and future directions for lower limb robotic exoskeletons. *IEEE Trans. Neural Syst. Rehabil. Eng.* **25**(2), 171–182 (2017). doi:10.1109/TNSRE.2016.2521160
6. Quinlivan, B., Lee, S., Malcolm, P., Rossi, D., Grimmer, M., Sivi, C., Karavas, N., Wagner, D., Asbeck, A., Galiana, I., *et al.*: Assistance magnitude versus metabolic cost reductions for a tethered multiarticular soft exosuit. *Sci. Robot.* **2**(2), 4416 (2017)
7. Asbeck, A.T., De Rossi, S.M., Holt, K.G., Walsh, C.J.: A biologically inspired soft exosuit for walking assistance. *Int. J. Robot. Res.* **34**(6), 744–762 (2015)
8. Kesar, T.M., Perumal, R., Reisman, D.S., Jancosko, A., Rudolph, K.S., Higginson, J.S., Binder-Macleod, S.A.: Functional electrical stimulation of ankle plantarflexor and dorsiflexor muscles: effects on poststroke gait. *Stroke* **40**(12), 3821–3827 (2009)
9. Embrey, D.G., Holtz, S.L., Alon, G., Brandsma, B.A., McCoy, S.W.: Functional electrical stimulation to dorsiflexors and plantar flexors during gait to improve walking in adults with chronic hemiplegia. *Arch. Phys. Med. Rehabil.* **91**(5), 687–696 (2010)
10. Sharma, N., Stegath, K., Gregory, C.M., Dixon, W.E.: Nonlinear neuromuscular electrical stimulation tracking control of a human limb. *IEEE Trans. Neural Syst. Rehabil. Eng.* **17**(6), 576–584 (2009)
11. Sharma, N., Gregory, C., Dixon, W.E.: Predictor-based compensation for electromechanical delay during neuromuscular electrical stimulation. *IEEE Trans. Neural Syst. Rehabil. Eng.* **19**(6), 601–611 (2011)
12. Alibeji, N., Kirsch, N., Farrokhi, S., Sharma, N.: Further results on predictor-based control of neuromuscular electrical stimulation. *IEEE Trans. Neural Syst. Rehabil. Eng.* (2015). doi:10.1109/TNSRE.2015.2418735
13. Hussain, S., Jamwal, P.K., Ghayesh, M.H., Xie, S.Q.: Assist-as-needed control of an intrinsically compliant robotic gait training orthosis. *IEEE Trans. Ind. Electron.* **64**(2), 1675–1685 (2016)
14. Selfslagh, A., Shokur, S., Campos, D.S., Donati, A.R., Almeida, S., Yamauti, S.Y., Coelho, D.B., Bouri, M., Nicoletis, M.A.: Non-invasive, brain-controlled functional electrical stimulation for locomotion rehabilitation in individuals with paraplegia. *Sci. Rep.* **9**(1), 1–17 (2019)
15. Wang, S., Wang, L., Meijneke, C., van Asseldonk, E., Hoellinger, T., Cheron, G., Ivanenko, Y., La Scaleia, V., Sylos-Labini, F., Molinari, M., Tamburella, F., Pisotta, I., Thorsteinsson, F., Ilzkovitz, M., Gancet, J., Nevatia, Y., Hauffe, R., Zanow, F., van der Kooij, H.: Design and Control of the MINDWALKER Exoskeleton. *IEEE Trans. Neural Syst. Rehabil. Eng.* **23**(2), 277–286 (2015). doi:10.1109/TNSRE.2014.2365697
16. Zanutto, D., Akiyama, Y., Stegall, P., Agrawal, S.K.: Knee Joint Misalignment in Exoskeletons for the Lower Extremities: Effects on User's Gait. *IEEE Trans. Robot.* **31**(4), 978–987 (2015). doi:10.1109/TRO.2015.2450414
17. Sartori, M., Farina, D., Lloyd, D.G.: Hybrid neuromusculoskeletal modeling to best track joint moments using a balance between muscle excitations derived from electromyograms and optimization. *J. Biomech.* **47**(15), 3613–3621 (2014). doi:10.1016/j.jbiomech.2014.10.009
18. Zhang, Q., Sheng, Z., Moore-Clingenpeel, F., Kim, K., Sharma, N.: Ankle dorsiflexion strength monitoring by combining sonomyography and electromyography. In: 2019 IEEE 16th International Conference on Rehabilitation Robotics (ICORR), pp. 240–245 (2019). IEEE
19. Han, J., Ding, Q., Xiong, A., Zhao, X.: A state-space emg model for the estimation of continuous joint movements. *IEEE Trans. Ind. Electron.* **62**(7), 4267–4275 (2015)

20. Batzianoulis, I., Krausz, N.E., Simon, A.M., Hargrove, L., Billard, A.: Decoding the grasping intention from electromyography during reaching motions. *J. NeuroEng. Rehabil.* **15**(1), 57 (2018). doi:10.1186/s12984-018-0396-5
21. Zhang, Q., Iyer, A., Sun, Z., Kim, K., Sharma, N.: A Dual-modal Approach Using Electromyography and Sonomyography Improves Prediction of Dynamic Ankle Dorsiflexion Motion. *IEEE Trans. Neural Syst. Rehabil. Eng.* **29**, 1944–1954 (2021)
22. Hargrove, L.J., Englehart, K., Hudgins, B.: A comparison of surface and intramuscular myoelectric signal classification. *IEEE Trans Biomed Eng* **54**(5), 847–853 (2007). doi:10.1109/TBME.2006.889192
23. Crouch, D.L., Pan, L., Filer, W., Stallings, J.W., Huang, H.: Comparing Surface and Intramuscular Electromyography for Simultaneous and Proportional Control Based on a Musculoskeletal Model: A Pilot Study. *IEEE Trans. Neural Syst. Rehabil. Eng.* **26**(9), 1735–1744 (2018). doi:10.1109/TNSRE.2018.2859833
24. Strasser, E.M., Draskovits, T., Praschak, M., Quittan, M., Graf, A.: Association between ultrasound measurements of muscle thickness, pennation angle, echogenicity and skeletal muscle strength in the elderly. *Age* **35**(6), 2377–2388 (2013). doi:10.1007/s11357-013-9517-z
25. Zhang, Q., Kim, K., Sharma, N.: Prediction of Ankle Dorsiflexion Moment by Combined Ultrasound Sonography and Electromyography. *IEEE Trans. Neural Syst. Rehabil. Eng.* **28**(1), 318–327 (2020)
26. Arampatzis, A., Karamanidis, K., Stafilidis, S., Morey-Klapsing, G., DeMonte, G., Brüggemann, G.-P.: Effect of different ankle-and knee-joint positions on gastrocnemius medialis fascicle length and emg activity during isometric plantar flexion. *J. Biomech.* **39**(10), 1891–1902 (2006)
27. Zhang, Q., Iyer, A., Kim, K., Sharma, N.: Evaluation of non-invasive ankle joint effort prediction methods for use in neurorehabilitation using electromyography and ultrasound imaging. *IEEE Trans. Biomed. Eng.* **68**(3), 1044–1055 (2021). doi:10.1109/TBME.2020.3014861
28. Damiano, D.L., Prosser, L.A., Curatalo, L.A., Alter, K.E.: Muscle plasticity and ankle control after repetitive use of a functional electrical stimulation device for foot drop in cerebral palsy. *Neurorehabil. Neural Repair* **27**(3), 200–207 (2013)
29. Hodson-Tole, E., Lai, A.: Ultrasound-derived changes in thickness of human ankle plantar flexor muscles during walking and running are not homogeneous along the muscle mid-belly region. *Sci. Rep.* **9**(1), 1–11 (2019)
30. Guo, J.-Y., Zheng, Y.-P., Xie, H.-B., Chen, X.: Continuous monitoring of electromyography (EMG), mechanomyography (MMG), sonomyography (SMG) and torque output during ramp and step isometric contractions. *Med. Eng. Phys.* **32**(9), 1032–1042 (2010). doi:10.1016/J.MEDENGGPHY.2010.07.004
31. Shi, J., Zheng, Y.P., Huang, Q.H., Chen, X.: Continuous monitoring of sonomyography, electromyography and torque generated by normal upper arm muscles during isometric contraction: Sonomyography assessment for arm muscles. *IEEE Trans. Biomed. Eng.* **55**(3), 1191–1198 (2008). doi:10.1109/TBME.2007.909538
32. Dick, T.J.M., Biewener, A.A., Wakeling, J.M.: Comparison of human gastrocnemius forces predicted by Hill-type muscle models and estimated from ultrasound images. *J. Exp. Biol.* **220**(9), 1643–1653 (2017). doi:10.1242/JEB.154807
33. Jahanandish, M.H., Fey, N.P., Hoyt, K.: Lower-Limb Motion Estimation Using Ultrasound Imaging: A Framework For Assistive Device Control. *IEEE J. Biomed. Health Inform.*, 1–10 (2019). doi:10.1109/jbhi.2019.2891997
34. Zhang, Q., Iyer, A., Kim, K., Sharma, N.: Volitional contractility assessment of plantar flexors by using non-invasive neuromuscular measurements. In: 2020 8th IEEE RAS/EMBS International Conference for Biomedical Robotics and Biomechanics (BioRob), pp. 515–520. IEEE
35. Zhang, Q., Clark, W.H., Franz, J.R., Sharma, N.: Personalized fusion of ultrasound and electromyography-derived neuromuscular features increases prediction accuracy of ankle moment during plantarflexion. *Biomed. Signal Process. Control* **71**, 103100 (2022)
36. Sikdar, S., Rangwala, H., Eastlake, E.B., Hunt, I.A., Nelson, A.J., Devanathan, J., Shin, A., Pancrazio, J.J.: Novel method for predicting dexterous individual finger movements by imaging muscle activity using a wearable ultrasonic system. *IEEE Trans. Neural Syst. Rehabil. Eng.* **22**(1), 69–76 (2013)
37. Dhawan, A.S., Mukherjee, B., Patwardhan, S., Akhlaghi, N., Diao, G., Levay, G., Holley, R., Joiner, W.M., Harris-Love, M., Sikdar, S.: Proprioceptive sonomyographic control: A novel method for intuitive and proportional control of multiple degrees-of-freedom for individuals with upper extremity limb loss. *Sci. Rep.* **9**(1), 1–15 (2019)
38. Sheng, Z., Sharma, N., Kim, K.: Quantitative assessment of changes in muscle contractility due to fatigue during nmes: An ultrasound imaging approach. *IEEE Trans. Biomed. Eng.* **67**(3), 832–841 (2019)
39. Lloyd, D.G., Besier, T.F.: An EMG-driven musculoskeletal model to estimate muscle forces and knee joint moments in vivo. *J. Biomech.* **36**(6), 765–776 (2003). doi:10.1016/S0021-9290(03)00010-1
40. Hodges, P.W., Pempel, L.H.M., Herbert, R.D., Gandevia, S.C.: Measurement of muscle contraction with ultrasound imaging. *Muscle & Nerve* **27**(6), 682–692 (2003). doi:10.1002/mus.10375
41. Shi, J., Zheng, Y.-P., Chen, X., Huang, Q.-H.: Assessment of muscle fatigue using sonomyography: muscle thickness change detected from ultrasound images. *Med. Eng. Phys.* **29**(4), 472–479 (2007)
42. McMeeken, J., Beith, I., Newham, D., Milligan, P., Critchley, D.: The relationship between emg and change in thickness of transversus abdominis. *Clin. Biomech.* **19**(4), 337–342 (2004)
43. Kiesel, K.B., Uhl, T.L., Underwood, F.B., Rodd, D.W., Nitz, A.J.: Measurement of lumbar multifidus muscle contraction with rehabilitative ultrasound imaging. *Man. Ther.* **12**(2), 161–166 (2007)
44. Zhang, Q., Fragnito, N., Myers, A., Sharma, N.: Plantarflexion Moment Prediction during the Walking Stance Phase with an sEMG-Ultrasound Imaging-Driven Model. In: 2021 Annual International Conference of the IEEE Engineering in Medicine and Biology Society (2021, Under review). IEEE
45. Delp, S.L., Anderson, F.C., Arnold, A.S., Loan, P., Habib, A., John, C.T., Guendelman, E., Thelen, D.G.: Opensim: open-source software to create and analyze dynamic simulations of movement. *IEEE Trans. Biomed. Eng.* **54**(11), 1940–1950 (2007)
46. Kainz, H., Hoang, H.X., Stockton, C., Boyd, R.R., Lloyd, D.G., Carty, C.P.: Accuracy and reliability of marker-based approaches to scale the pelvis, thigh, and shank segments in musculoskeletal models. *J. Appl.*

- Biomech. **33**(5), 354–360 (2017)
47. Scott, S.H., Winter, D.A.: A comparison of three muscle pennation assumptions and their effect on isometric and isotonic force. *Journal of biomechanics* **24**(2), 163–167 (1991)
 48. Epstein, M.: Theoretical models of skeletal muscle: biological and mathematical considerations. John Wiley & Sons, 52–53 (1998)
 49. Guimaraes, A., Herzog, W., Hulliger, M., Zhang, Y., Day, S.: Effects of muscle length on the emg-force relationship of the cat soleus muscle studied using non-periodic stimulation of ventral root filaments. *J. Exp. Biol.* **193**(1), 49–64 (1994)
 50. Huijing, P.A.: Important experimental factors for skeletal muscle modelling: non-linear changes of muscle length force characteristics as a function of degree of activity. *Eur. J. Morphol.* **34**(1), 47–54 (1996)
 51. Zajac, F.E.: Muscle and tendon: properties, models, scaling, and application to biomechanics and motor control. *Crit Rev Biomed Eng* **17**(4), 359–411 (1989)
 52. Ao, D., Song, R., Gao, J.: Movement Performance of Human-Robot Cooperation Control Based on EMG-Driven Hill-Type and Proportional Models for an Ankle Power-Assist Exoskeleton Robot. *IEEE Trans. Neural Syst. Rehabil. Eng.* **25**(8), 1125–1134 (2017)
 53. Farris, D.J., Lichtwark, G.A.: UltraTrack: Software for semi-automated tracking of muscle fascicles in sequences of B-mode ultrasound images. *Comput. Methods Programs Biomed.* **128**, 111–118 (2016). doi:10.1016/J.CMPB.2016.02.016
 54. Yamaguchi, G.: A survey of human musculotendon actuator parameters. *Multiple muscle systems: Biomechanics and movement organization* (1990)
 55. MacLean, M.K., Ferris, D.P.: Human muscle activity and lower limb biomechanics of overground walking at varying levels of simulated reduced gravity and gait speeds. *PloS one* **16**(7), 0253467 (2021)
 56. Liu, M.M., Herzog, W., Savelberg, H.H.C.M.: Dynamic muscle force predictions from EMG: an artificial neural network approach. *J. Electromyogr. Kinesiol.* **9**(6), 391–400 (1999). doi:10.1016/S1050-6411(99)00014-0
 57. Barbero, M., Merletti, R., Rainoldi, A.: Atlas of Muscle Innervation Zones: Understanding Surface Electromyography and Its Applications. Springer, ??? (2012). doi:10.1007/978-88-470-2463-2
 58. Aagaard, P., Andersen, J.L., Dyhre-Poulsen, P., Leffers, A.-M., Wagner, A., Magnusson, S.P., Halkjær-Kristensen, J., Simonsen, E.B.: A mechanism for increased contractile strength of human pennate muscle in response to strength training: changes in muscle architecture. *J. Physiol.* **534**(2), 613–623 (2001)
 59. Schmitz, A., Silder, A., Heiderscheit, B., Mahoney, J., Thelen, D.G.: Differences in lower-extremity muscular activation during walking between healthy older and young adults. *J. Electromyogr. Kinesiol.* **19**(6), 1085–1091 (2009)

belts and in-ground force plates. (2) 39 retro-reflective markers on participant's

lower body for lower limb kinematics measurements. (3) A single US transducer to image both LGS and SOL muscles with the appropriate probe placement. (4) Four sEMG sensors to record signals from LGS, MGS, SOL, and tibialis anterior muscles. (5) Ultrasound imaging machine to collect radio frequency data. (6) Computer screen to show B-mode ultrasound imaging. (7) Computer screen to show live markers and segment links of the participant. (8) 12 motion capture cameras to track markers' trajectories. (b) Schematic illustration of the proposed sEMG-US imaging-driven HNM calibration. The weighted muscle activation for LGS or SOL combines both sEMG signals and US imaging. Red solid, black solid, and blue dashed lines with an arrow represent the input signals to HNMs, the intermediate sub-model output signals, and the unknown parameters adjustment, respectively.

Figure 3

SOL muscle thickness tracking results by using UltraT rack at different walking speeds on Participant Sub08. Each subplot represents

the tracking results during the recorded 20 s experiments under each walking speed, and the red solid and blue dashed lines represent the results with and without key-frame correction, respectively.

Figure 4

Results of joint kinematics, kinetics, and neuromuscular features during the treadmill walking experiments at different speeds on Participant Sub01. (a) Mean and one SD of right ankle joint kinematics and kinetics data during recorded gait cycles (between two successive heel-strike time instants). (b) Mean and one SD of plantarflexors' neuromuscular features from

processed sEMG signals and US imaging signals during recorded stance phase cycles (from heel-strike to toe-off within the same gait cycle). The solid lines report the mean values, while the light shadowed areas report one SD values of each variable.

Figure 5

Calibration results by using three HNM categories on Participant Sub05 under single-speed modes. The calibration performance by using sEMG-, US imaging-, and sEMG-US imaging-driven HNMs under 5 single

speed modes on Sub05. The red lines and light shadowed areas represent the mean and SD of the net PF moment from the ID calculation, the blue, green, black lines and light shadowed areas represent the mean and SD of the net PF moment from calibrations by using sEMG-driven HNM, US imaging-driven HNM, and sEMG-US imaging-driven HNM, respectively. (a)-(e) represent the results at each walking speed from 0.50 m/s to 1.50 m/s.

Figure 6

Calibration performance across all participants by using three HNM categories. The mean and SD of BM-RMSE, N-RMSE and R2 values across all participants under both single-speed modes are displayed in upper, middle, and lower plots, respectively, during calibration procedures. Blue, red, and yellow bars represent the result by using sEMG-, US imaging-, and sEMG-US imaging-driven HNMs, respectively.

Figure 7

Prediction performance across all participants by using three HNM categories. The mean and SD of BM-RMSE, N-RMSE and R2 values across all participants under both single-speed modes and inter-speed model are displayed in upper, middle, and lower plots, respectively.

Blue, red, and yellow bars represent the prediction result by using sEMG-, US imaging-, and sEMG-US imaging-driven HNMs, respectively. Column subplots from left to right represent that these applied HNMs were calibrated under single-speed modes (0.50 m/s, 0.75 m/s, 1.00 m/s, 1.25 m/s, and 1.50 m/s) and the inter-speed mode.

Supplementary Files

This is a list of supplementary files associated with this preprint. Click to download.

- [Supplementarymaterials.pdf](#)
- [sub010.5fasciclevideo.avi](#)
- [sub010.75fasciclevideo.avi](#)
- [sub011.0fasciclevideo.avi](#)

- sub011.25fasciclevideo.avi
- sub011.5fasciclevideo.avi